In situ characterisation of surface roughness and its amplification during multilayer single-track laser powder bed fusion additive manufacturing

Alisha Bhatt [a,b,f,g,*], Yuze Huang [a,b,c], Chu Lun Alex Leung [a,b,*], Gowtham Soundarapandiyan [c,d], Sebastian Marussi [a,b], Saurabh Shah [a,b], Robert C. Atwood [e], Michael E. Fitzpatrick [c], Manish K. Tiwari [a,f,g], Peter D. Lee [a,b,*]

[a] *Department of Mechanical Engineering, University College London, Torrington Place, WC1E 7JE London, UK*
[b] *Research Complex at Harwell, Harwell Science & Innovation Campus, OX11 0FA Didcot, UK*
[c] *Faculty of Engineering, Environment and Computing Coventry University, CV1 5FB Coventry, UK*
[d] *National Structural Integrity Research Centre (NSIRC), Granta Park, CB21 6AL Cambridge, UK*
[e] *Diamond Light Source Ltd, Diamond House, Harwell Science & Innovation Campus, OX11 0DE Didcot, UK*
[f] *Nanoengineered Systems Laboratory, University College London, Torrington Place, WC1E 7JE London, UK*
[g] *EPSRC Centre for Interventional and Surgical Sciences (WEISS), University College London, W1W 7TS London, UK*

ARTICLE INFO

ABSTRACT

Surface roughness controls the mechanical performance and durability (*e.g.,* wear and corrosion resistance) of laser powder bed fusion (LPBF) components. The evolution mechanisms of surface roughness during LPBF are not well understood due to a lack of *in situ* characterisation methods. Here, we quantified key processes and defect dynamics using synchrotron X-ray imaging and *ex situ* optical imaging and explained the evolution mechanisms of side-skin and top-skin roughness during multi-layer LPBF of Ti-6Al-4V (where down-skin roughness was out of the project scope). We found that the average surface roughness alone is not an accurate representation of surface topology of an LPBF component and that the surface topology is multimodal (*e.g.,* containing both roughness and waviness) and multiscale (*e.g.,* from 25 μm sintered powder features to 250 μm molten pool wavelength). Both roughness and topology are significantly affected by the formation of pre-layer humping, spatter, and rippling defects. We developed a surface topology matrix that accurately describes surface features by combining 8 different metrics: average roughness, root mean square roughness, maximum profile peak height, maximum profile valley height, mean height, mean width, skewness, and melt pool size ratio. This matrix provides a guide to determine the appropriate linear energy density to achieve the optimum surface finish of Ti-6Al-4V thin-wall builds. This work lays a foundation for surface texture control which is critical for build design, metrology, and performance in LPBF.

1. Introduction

Laser powder bed fusion (LPBF) additive manufacturing (AM) is a digital manufacturing process that produces complex metallic components with excellent mechanical properties owing to the grain structure and reduction in phase segregation under rapid solidification [1–3]. The "as-built" LPBF parts often exhibit rough surfaces [4], requiring additional post-processing steps to achieve a desired surface finish [5]: this increases lead time and development cost. Many post-processing methods, including heat treatment [6], hot isotropic pressing [7], ultrasonic nanocrystal surface modification [6], advanced finishing

machining [8] and laser polishing [9], have been used to improve the surface finish and eliminate residual stresses in "as-built" components [10]. Roughness control on AM parts is vital as surface roughness has its advantages and disadvantages depending on the end-user applications, *e.g.* controlled roughness can promote bond formation between implants and the human body [11,12], whereas surface irregularities can lead to wear or reduction in fatigue life and consequently lower the part performance [13].

The surface finish of the AM part is governed by process parameters (*e.g.* laser power, scan speed, hatch distance, and layer thickness, *etc.*) and materials parameters (*e.g.* optical and thermophysical properties)

[14,15]. In general, the surface roughness decreases with increasing laser power (*P*) and reducing scan speed (*v*) [14,16,17]. Conversely, lower heat input or linear energy density (LED = *P/v*) applied to the powder bed leads to a colder and more viscous melt pool, promotes poor wetting behaviour [14], and results in balling-like features and increased surface roughness [18]. These prior studies predominantly studied LED ranges from 0.1 to 1.5 Jmm^{-1} [14,18,19].

Several characterisation techniques have been used to quantify the surface roughness of AM components, including optical microscopy [20], scanning electron microscopy (SEM) [19], atomic force microscopy [21], coherence scanning interferometry (CSI) [14], and hyperspectral imaging [22]. None of these techniques can study the built topology on a layer-by-layer basis; therefore, the underlying mechanisms in which both geometrical properties and individual powder layer thickness contribute to the final build part remain unclear. Analysing the interlayer roughness and quantifying the underlying mechanisms would provide further insight to achieve optimum as-built surface quality.

Engineering surface textures are split into three key profiles: roughness, waviness, and nominal profile [23]. Roughness refers to micro-scaled asperities of the build surface, also known as fine textures [24]. Fine textures are usually generated by the laser beam melting or sintering of powder particles [25]. Roughness parameters are measured commonly in a two-dimensional form (2D) and they are typically used to dictate the overall surface roughness topology [26]. Amplitude parameters are commonly used to describe the surface topology by quantifying the vertical surface deviation with respect to a centre line [27]. R_a, the average surface roughness, is also known as the arithmetic average of the profile height deviation from the centre line, *i.e.*, the mean height which indicates the overall surface texture [28]. Surface waviness describes the periodic oscillations induced by the melt pool behaviour [29]: it usually increases with a decrease in surface roughness. Lastly, the nominal profile is described as a combination of the roughness and waviness profile.

To produce high-quality AM parts, *in situ* monitoring can help achieve the desired surface texture [20,30]. *In situ* optical and thermographic imaging studies focus on surface roughness at the final build layer which does not reveal the interlayer mechanisms that lead to some types of surface roughness [31,32]. New analysis methods are required to understand both final build layer and interlayer relationships. To characterise surface roughness for a multilayer build, various statistical parameters should be used such as average roughness (R_a), root mean square (*RMS*), and skewness (*Sk*) [24,26], which in return provides a feedback system for monitoring surface roughness through parameter control as demonstrated by ref.[26].

Synchrotron radiation enables X-ray imaging to offer unparalleled spatial and temporal resolution [33]. Several research groups have used *in situ* X-ray imaging to study process dynamics during multilayer LPBF [30,34,35] but have not discussed the underlying mechanisms involved in surface roughness variations under multilayer conditions. The first multilayer X-ray imaging study of LPBF [34] revealed that a thick powder layer could increase spatter, whereas a thin powder layer could lead to laser remelting, forming a smoother track surface.

Recent work shows that increasing the imparted specific energy, SE $= \frac{P}{(v.d)^{0.5}}$(MJm^{-1}s$^{-\frac{1}{2}}$) [36], where *P* is power, *v* is scan speed, and *d* is the beam diameter, reduces surface roughness and increases waviness [37]. The resultant surface topology of an AM track is linked to the hump formation owing to the combination of Plateau-Rayleigh and Kelvin-Helmholtz instabilities. The variations in *v* and *P* under overhang conditions also impact the laser energy transferred to the powder particles, thus having a direct influence on the melt pool size and wetting mechanisms which lead to balling phenomena by reducing laser power and scan speed.

Although X-ray imaging has been used to analyse multilayer LPBF of Ti-6Al-4V where the surface texture and overall topology of the thin-wall builds are linked to the powder layer thickness, the underlying evolution mechanisms that lead to different degrees of surface roughness are not yet known [38]. Here, we characterise and quantify multilayer LPBF builds using *in situ* high-speed synchrotron X-ray radiography coupled with an *in situ* and *in operando* process replicator (ISOPR) [39]. We successfully captured the evolution of processing defects (*e.g.* porosity and spatter) and surface texture in thin-wall builds composed of 10 layers under eight different linear energy densities LEDs. Post-mortem analysis was carried out to further examine the overall internal defects using X-ray computed tomography (XCT) and high-resolution surface profiling to validate *in situ* measurements. We also investigate the relationship between surface roughness and LED, quantifying the interlayer underpinning mechanisms that result in the final surface roughness of the build and delivering a roughness selection matrix to optimise the topology of the built part. The impact of this work can improve surface texture control in LPBF and could be further extended to welding and other laser processing technologies.

2. Materials and methods

Ti-6Al-4V powder (TLS Technik GmbH & Co. Spezialpulver KG, Germany) with a nominal size range of 24–68 μm, $D_{V(10)} = 26$ μm, $D_{V(50)} = 38$ μm and $D_{V(90)} = 55$ μm (shown in Supplementary Fig. 1 and Supplementary Table. 1) and 1-mm-thick Ti-6Al-4V alloy substrates were used for the *in situ* multilayer build during the LPBF experiments.

2.1. In situ X-ray imaging of LPBF

Here, the LPBF experiments were conducted using an *in situ* and *in operando* process replicator (ISOPR) [39], which was designed to mimic the major features of an LPBF system which consists of a 200 W, 1030–1070 nm, continuous wave fibre laser with a spot size of 50 μm. The powder bed was filled with gas-atomised Ti-6Al-4V powder, which was fused in the environmental chamber which consists of an automated powder hopper, sample holder, and argon gas pressure sensor. The environmental chamber was sealed and backfilled with argon at a flow rate of 4 lmin^{-1} and then evacuated. The system chamber has two X-ray windows which are made of glassy carbon. This device can operate as a standalone unit and is also integrable into different synchrotron beamlines [40]. The process parameters are given in Supplementary Table 2 with LED ranging from 0.5 to 4 Jmm^{-1}. Each build is 5 mm long with a total of 10 fused powder layers (Supplementary Fig. 2) with a nominal 100 μm thickness [41] under a bi-directional scanning strategy [30]. X-ray imaging was performed at the beamline I12: Joint Engineering, Environmental, and Processing (JEEP), Diamond Light Source, UK [33, 37].

2.2. Surface roughness measurements

Fiji version 1.52i [42], Python 3.7 [43,44] and MATLAB 2019a [45] were used to analyse the radiographs. A flat-field correction (FFC) was applied to the radiographs before analysis to reduce noise introduced by the detector and distortions in the optical beam path, improving the overall image quality [46,47]. FFC is used to renormalise intensities across the image and correct the intensity pattern (Fig. 1a). A standard FFC equation is deployed using a Python script, and image denoising was run using the VBM3D method depicted in ref.[39,48]. Denoising allowed a clearer segmentation between the melt track, background (argon), and powder. After that, Otsu thresholding was applied to the denoised image to segment the background and melt track [49] (Fig. 1b-c). We used the binarised image to calculate the built height by adding all the pixels in the build direction along the track length forming a track profile using a MATLAB script [50] (Fig. 1di). Using the Gaussian filtering process, a high-pass filter is applied to separate the roughness profile using a MATLAB script ref.[51], Ga(x) $= \frac{1}{\alpha\lambda c}\exp\left[-\pi\left(\frac{1}{\alpha\lambda c}\right)^2\right]$ [52] where $\alpha = \sqrt{\ln 2}/\pi$, x is the position from the origin of the weighted
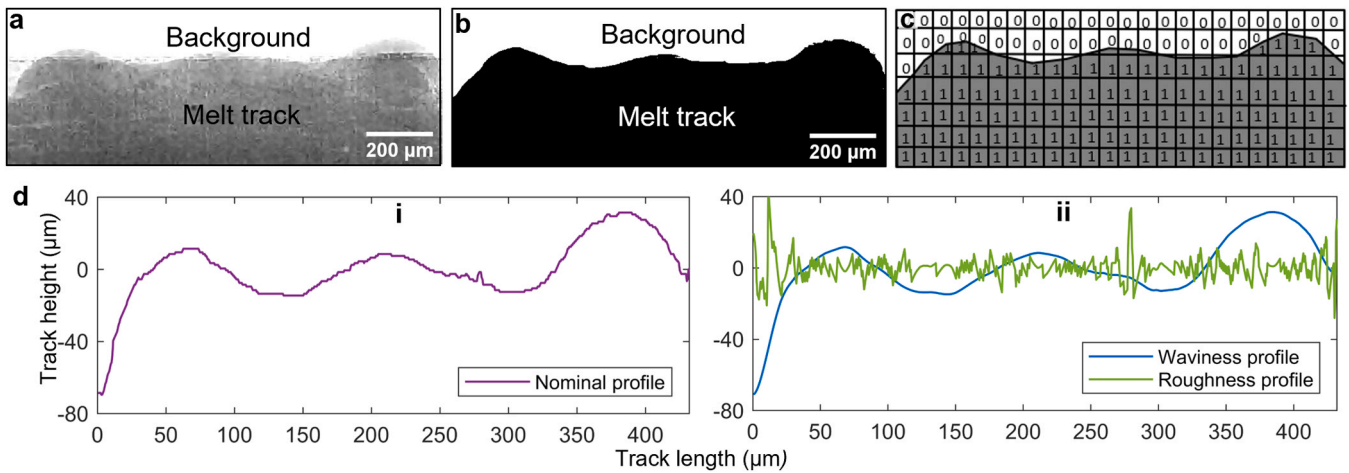
Fig. 1. Time series radiograph acquired during deposition of a single track during multilayer thin-wall build LPBF process for Ti-6Al-4V under $P = 200$ W and $v = 50$ mms^{-1} for the 10th layer. a) Raw image that has been flat field corrected and denoised, b) adaptive threshold cropping of the relevant section, c) schematic of the image matrix which has been binarized and d) track profile extraction with the use of a Gaussian filter to split the key engineering textures (waviness and roughness).

function, and λ_c is the long-wavelength also known as the roughness cut-off. The cut-off frequency for the filter is denoted by the nominal size range of the Ti-6Al-4V powder (Supplementary Table 1). The Gaussian filter is commonly used and recommended by the ISO 11562–1996 and ASME B46–1995 standards for the roughness analysis [53]. The surface roughness and waviness were then extracted (see inset Fig. 1dii) [54]. All initial *in situ* data analysis was conducted using Image J (Fiji version 1.52i) before deploying any Python or MATLAB script for validation purposes. After *in situ* experiments, the surface roughness of all samples was non-destructively examined and imaged by a high-resolution optical microscope (Keyence VHX-7000, Keyence, Japan) [33] to allow consistent measurements. Most defects imaged by optical microscopy were greater than 60 µm therefore sub-micron imaging, such as SEM was

not required for this study. The autofocus [55] setting for the optical microscope is used to focus on the defect imaged solely, which results in blurring of other (not relevant) features due to the sample not being completely flat.

2.3. X-ray computed tomography (XCT) analysis

To quantify the trapped powder between melt tracks, we performed XCT scans on the thin walls produced from the *in situ* experiments using a Nikon XTH 225 X-ray microfocus tomography system. Each scan consisted of 3175 projections with 1 s exposure time [30,37]. The data were reconstructed (with a voxel size of 2.7 µm) and analysed using the method presented in ref [30]. XCT was used alongside optical
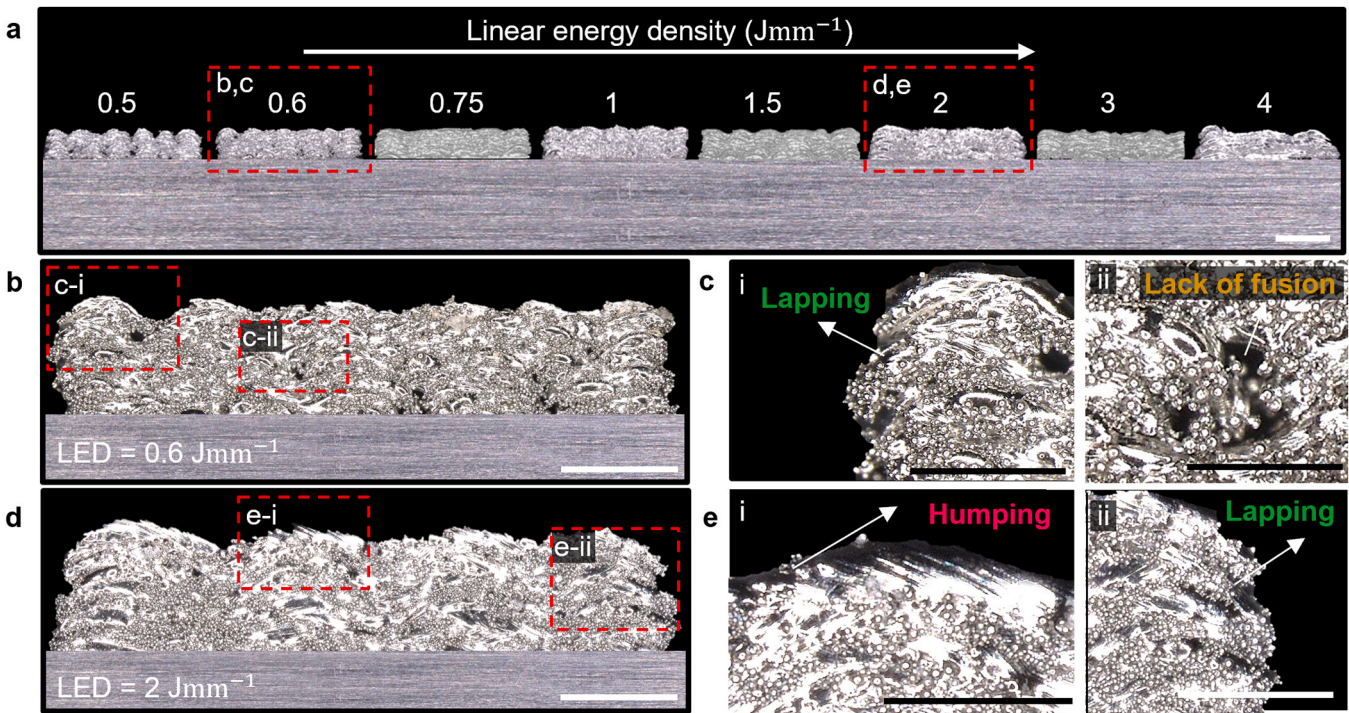

Fig. 2. a) Ti-6Al-4V multilayer thin builds made by LPBF under 8 different linear energy densities (LED), ranging from 0.5 to 4 Jmm^{-1}. b). LED = 0.6 Jmm^{-1} thin-wall structure with c-i) lapping and c-ii) lack of fusion defects. D) LED = 2 Jmm^{-1} thin wall structure with. e-i) humping and e-ii) lapping defects. All scale bars are 200 µm.

microscopy and *in situ* X-ray radiographs for further validation of lapping defects.

3. Results and discussion

3.1. Top surface defects revealed by the surface profile/morphology

High-resolution optical images of the thin-wall builds are shown in Fig. 2. The results highlight the presence of various surface defects after multilayer LPBF for 8 different LEDs. Fig. 2a shows that the size of the waviness (λ) increases with LED. At an LED of 0.5–0.6 Jmm^{-1} and under a scan speed of 300–400 mms^{-1}, we observe track interruption with low λ, and balling defects owing to insufficient melting [56] and poor wetting resulting in an increased solidification rate and thus the formation ellipsoidal balling.

As the scan speed further decreases, while keeping a constant laser power, the LED increases (up to 1 Jmm^{-1}), the top profile of the thin walls is flattened, and the surface humps are drastically reduced. With a further increase of LED from 1.5 to 4 Jmm^{-1}, the top profile of the thin wall becomes wavier. At an LED of 4 Jmm^{-1}, more prominent lamellar rippling is found on the melt track, which is similar to the defect reported in welding [57].

We have identified three types of defects in these thin walls: (1) lapping defects (Fig. 2b and further discussed in Fig. 4c) are found at both ends of all builds between built layers (as shown by the inset in Fig. 2-i and Fig. 2e-ii) under the conditions studied; (2) lack-of-fusion defects are found with unsintered powder, indicating insufficient energy was applied at the powder bed at an LED of 0.5–0.6 Jmm^{-1} (Fig. 2c-ii); and (3) humps, swell-like defects (Fig. 2d), mainly form as λ increases with non-optimal LED, *e.g.* < 0.75 and > 1 J mm^{-1} (Fig. 2e-i) [38].

In LPBF, the print quality of each layer has a direct effect on subsequent layers, and hence the overall build morphology. To further understand the impact of lapping, hump formation and lack-of-fusion defects on the side-skin roughness of the thin wall, we studied the evolution of these defects during LPBF over 10 build layers using *in situ* synchrotron X-ray imaging, see details in Sections 3.2 – 3.4, respectively.

Three LED conditions were selected that show track interruption (Fig. 3a), rippling (Fig. 3b) and necking effect (Fig. 3c) at the top surface of the thin-wall build (see other thin-wall profiles at different LEDs in Supplementary Fig 3).

At an LED of 0.5 Jmm^{-1}, track interruption and balling are prevalent due to the higher surface tension at a lower melt temperature, leading to incomplete melting (Fig. 3a). Additionally, the sintered powder is observed between humps due to spattering during LPBF.

At an LED of 2 Jmm^{-1} the surface tension gradient from the centre to the edge of the melt pool will be higher, and this may also lower the melt viscosity, creating a higher Marangoni-driven flow towards the pool edge [58], which freezes in as ripples at the rear of the pool, resulting in higher top-skin roughness but a continuous track (Fig. 3b).

With a further increase of LED from 2 to 4 Jmm^{-1}, necking is more prevalent (Fig. 3c), reaching a threshold linear energy density which deteriorates the build quality. Supplementary Table 2 confirms that the stable rippling and necking under an LED of 4 Jmms^{-1} and our observations are consistent with prior studies [59] where neck formation was

due to the Plateau-Rayleigh instability.

3.2. Lapping formation revealed by in situ synchrotron X-ray imaging

Lapping affects both geometrical properties and mechanical properties of the build [60], which is observed at both ends of the final multilayer builds under all the conditions studied, shown in Fig. 2d-i and Fig. 2f-ii. Using synchrotron X-ray imaging, we captured the lapping evolution mechanism during LPBF. Fig. 4a shows a radiograph of a thin-wall build after the 10th layer, wherein the light grey lines at the ends of the track are labelled as lapping. The grey scale values indicate how much energy has been attenuated along the X-ray beam path: the lighter the pixel, the less energy is being attenuated by the object and darker pixels indicate higher attenuation.

The radiograph (Fig. 4a-ii), optical (Fig. 4b), and XCT 3D rendering images (Fig. 4c) confirm the presence of sintered powder between the overlapping tracks. The *in situ* X-ray images (Fig. 4d-g) have allowed us to capture, for the first time, how a lapping defect is formed under a multilayer LPBF process. Firstly, the layer thickness increases by powder accumulation at the edge of the previously solidified structure: this alters the build condition from remelting to an overhang build condition (Fig. 4d). At the onset of the melting process, the effective thermal conductivity of the Ti-6Al-4V reduces up to 90% [61]: this promotes the formation of balling or melt pool curl-up on the accumulated powder [39] (see Fig. 4e). The liquid metal may overflow, wet onto the solidified structure below, and subsequently trap powder particles whilst merging with the solidified part. In other words, the powder particles are sandwiched by two scan tracks above and below, forming the lapping defect (Fig. 4f). As the laser beam continues to move from right to left, the layer thickness is reduced from 100 μm to none, indicating significant remelting and promoting a large volume of melt flowing towards the end of the track, such that the added material warps or budges upwards as it cools. (Fig. 4g).

3.3. Lack-of-fusion porosity revealed by in situ synchrotron X-ray imaging

Lack-of-fusion porosities are only observed during LPBF at a low LED of 0.5 – 0.6 Jmm^{-1}. We selected an LED of 0.5 Jmm^{-1} to explore the underlying defect evolution mechanisms, see Fig. 5a. Fig. 5b and c show two types of lack of fusion: (Type I) between two humps and (Type II) within the build, respectively. To analyse how lack-of-fusion porosities arise, we quantified the grey colour variation at the region of interest from layer 5 (Fig. 5d) and subsequent build layers (Fig. 5e). By measuring the 2D projected build area from the radiographs, there are up to 6% more light grey pixels in the thin wall structure as the build layer increases from 5 to 10, *i.e.*, showing more unmelted powder, or lack-of-fusion porosity, which correlates with Fig. 5a. From our observations, the warping/bulging effect (depicted in Section 3.2) becomes more prominent, forming peaks (where materials build) and troughs (filled with sintered powder). The powder particles at the trough region are being ejected by the metal vapour as the laser beam remelts the peak material, leaving a gap between two humps, *i.e.*, type I lack-of-fusion porosity. On some occasions, not all powder particles are ejected: instead, they undergo partial melting and form weak interconnects between humps, *i.e.*, type II lack-of-fusion porosity.
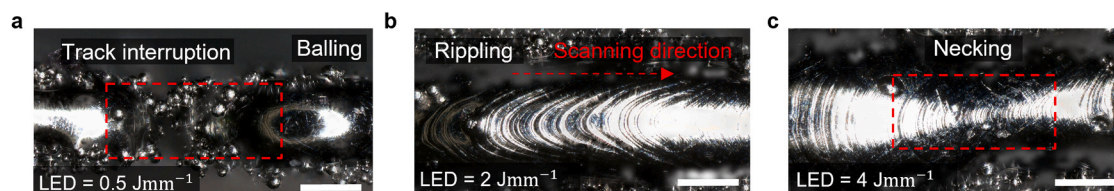

Fig. 3. Optical images of Ti-6Al-4V multilayer thin wall builds by laser powder bed fusion (other LED conditions in Supplementary Fig 3). a Track interruption and balling observed at 0.5 Jmm^{-1}. b Rippling observed at 2 Jmm^{-1} against the scanning direction. c Necking observed at 4 Jmm^{-1}. All scale bars are 200 μm.
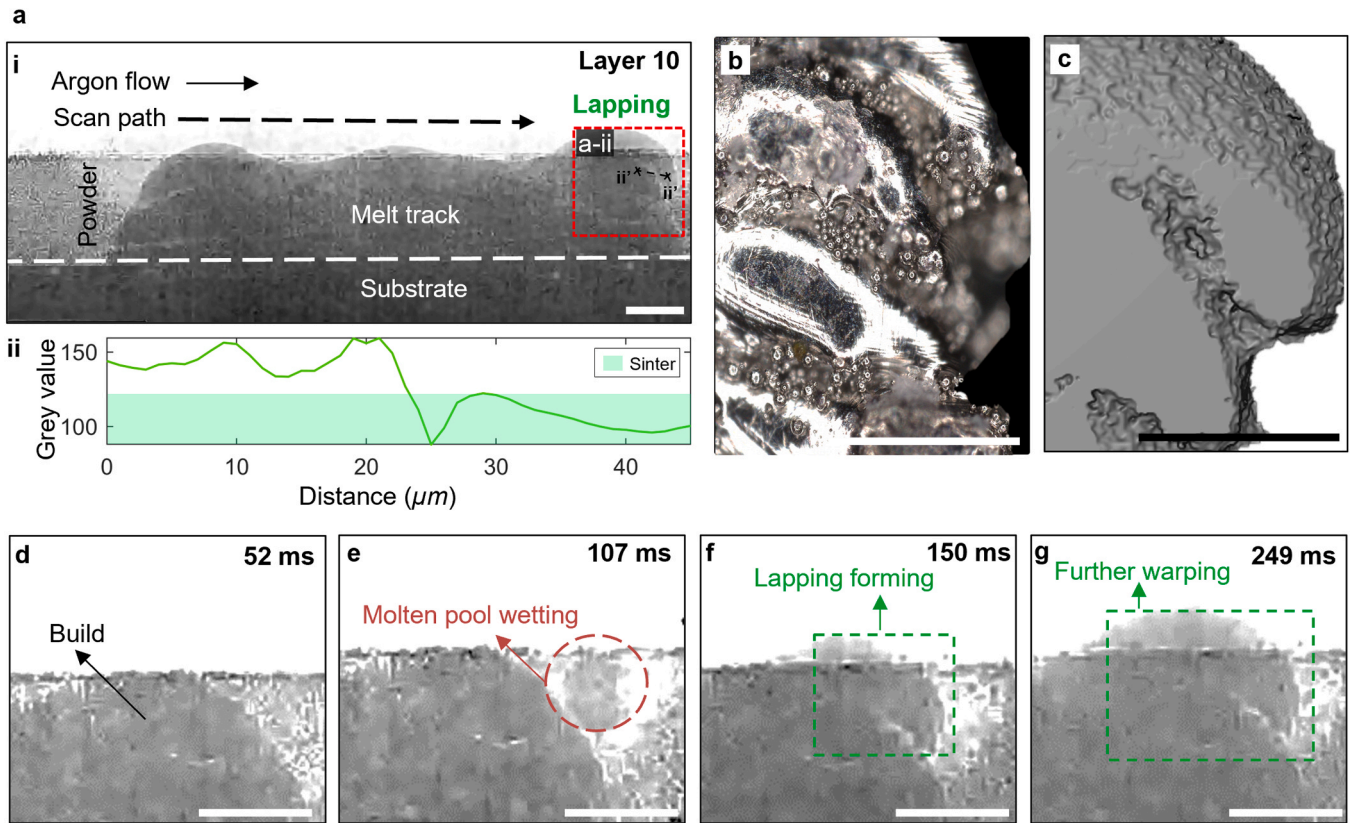
Fig. 4. Synchrotron X-ray radiographs acquired during multilayer TI-64-Al-4V builds in laser powder bed fusion under a power $P = 200$ W, a scan speed $v = 50$ mms^{-1} and a linear energy density LED= 4 Jmm^{-1} (Supplementary video 1). a-i) Radiograph of the melt track for the final morphology at the 10th layer, black arrows indicate the scanning directions and argon flow. a-i) the lapping region and a-ii) greyscale intensity profile. b) Optical image of the lapping region showing the lapping defect and c) XCT of the multi-build showing the lapping defect. d-g) The evolution of the lapping defect revealed by synchrotron X-ray imaging for layer 8. The green and red shaded regions correspond to lapping and melt pool wetting, respectively. All scale bars are 100 μm.
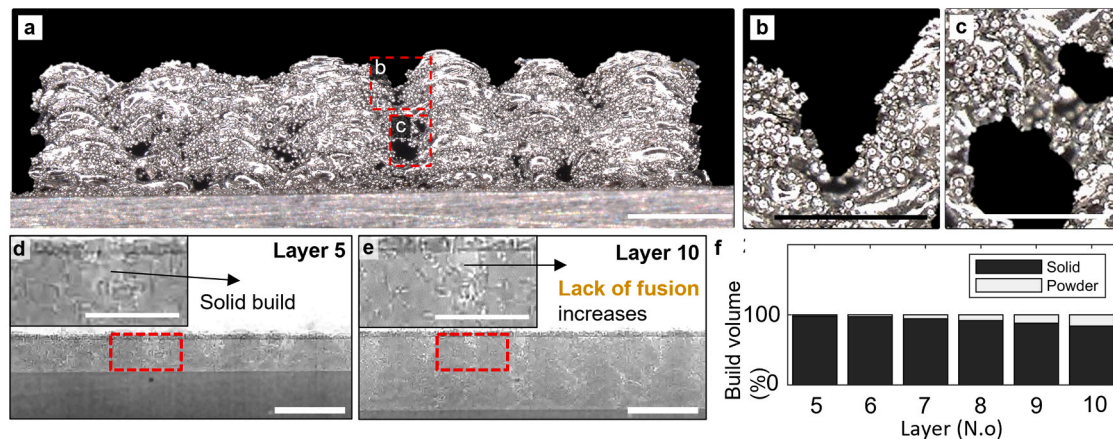

Fig. 5. Synchrotron X-ray radiographs acquired during laser powder bed fusion with laser power $P = 200$ W, scan speed $v = 400$ mms^{-1} and linear energy density LED= 0.5 Jmm^{-1}. a) Multi build profile (ex situ) of 10 layers. b) Lack of fusion between humps. c) Lack of fusion porosity within the build. d-e) Evolution of lack of fusion porosity from layers 5–10 as seen in (Supplementary Fig. 5a-f, Supplementary videos 2 and video 3). f) Plot for layers 5–10 shows the growth of powder within the build volume indicating lack of fusion (Supplementary Fig. 5 g). All scale bars are 200 μm.

Supplementary material related to this article can be found online at doi:10.1016/j.addma.2023.103809.

3.4. Spatter defects revealed by in situ synchrotron X-ray imaging

At an LED of 0.5 J mm^{-1}, the melt pool is expected to have a low average temperature and thermal gradient, resulting in a higher surface tension compared to the melt pool processed at a higher LED. The melt pool size is also expected to have a smaller depth (d) and width (w) at this LED. This high surface tension and low melt pool (d/w) aspect ratio causes the melt pool to undergo Plateau–Rayleigh instability, forming melt beads rather than continuous melt track (at 66 ms). The ejection of a melt bead is seen at 246 ms, which subsequently lands on the powder bed (at 812 ms), see Fig. 6a. This solidified bead could potentially create
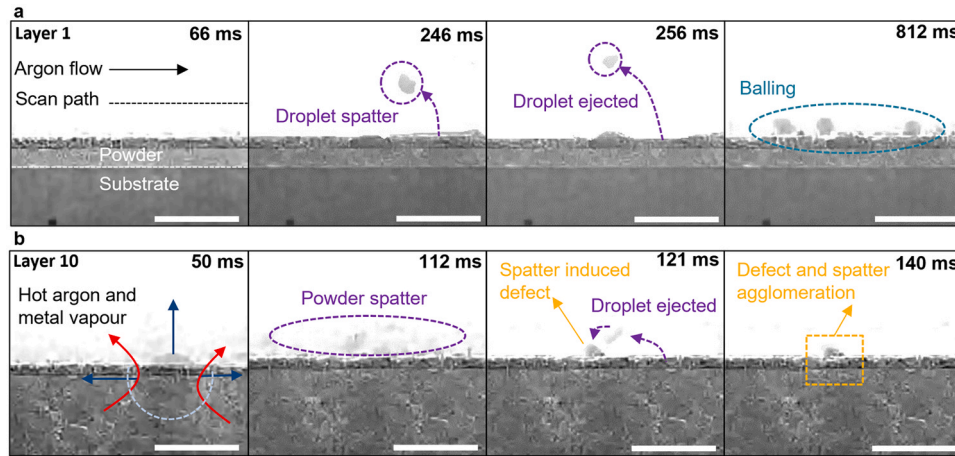
Fig. 6. Synchrotron X-ray radiographs acquired during laser powder bed fusion with laser power $P = 200$ W, scan speed $v = 400$ mms^{-1} and linear energy density LED= 0.5 Jmm^{-1} (Supplementary videos 3 and 4). Spatter and balling evolution were revealed for a) layer 1 and b) layer 10 resulting in lack of fusion within the build as presented in the final morphology in Fig. 5. All scale bars are 100 μm.

a defect in subsequent tracks.

Fig. 6b shows that the formation of powder spatter is due to hot particles or solidified beads (Fig. 6a) being ejected from metal vaporisation at the melt pool surface (at 50 ms) [39,62]. Unlike what has been reported, we observed the formation of large droplet spatter could also be caused by the agglomeration of powder (112 ms) and droplet spatter (121 ms). These droplet spatters (Fig. 6a-b) may land and solidify on the melt track and result in a high side-skin roughness.

3.5. Humping defect revealed by in situ synchrotron X-ray imaging

Under all conditions studied, we observe hump formation at the end of the track, which could be due to a combination of the lapping defect (depicted in Section 3.2) and deceleration of the scanning mirror in the LPBF system [63]. On the other hand, we periodically observed humping defects in the middle of the build under non-optimal conditions (Fig. 5).

Here, we selected the thin-wall sample made with LED of 1.5 Jmm^{-1} for the following discussion. Fig. 7a shows the side view of the thin wall after a 10-layer build. The zoom-in images show that there are regular large humps (Fig 7bi) and irregular small humps (Fig 7ci). Fig. 7a shows a qualitative increase in powder denudation on the side-skin (front surface in Fig. 7) of the track in comparison to a lower LED build in Fig. 5a. Although not quantified, this result qualitatively matches the results of ref. [64], shows a transition from significant balling and spatter causing significant rough powder attachment at the side surface of the build (front of Fig. 5a) as compared to the large pool with a smoother track side surface with little powder attachment, albeit with greater waviness on the top surface. To understand how these humps formed during LPBF, we looked into the time-series radiographs. As the moving laser beam melts the powder and substrate, the liquid metal is moving backwards, adding material at the end of the track, and forming a hump (Fig 7bii). We hypothesise that the humps (seen at 123 ms) were
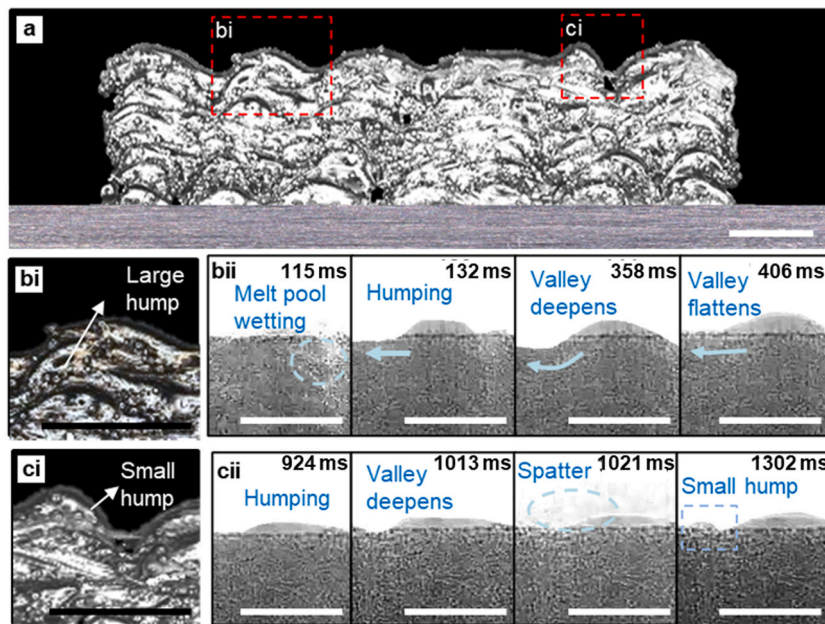

Fig. 7. Synchrotron X-ray radiographs acquired during laser powder bed fusion of TI-64-Al-4V under a laser power $P = 150$ W, scan speed $v = 50$ mms^{-1} and linear energy density LED = 1.5 Jmm^{-1}, see details in Supplementary video 5. a) Side view of the thin wall structure after 10 build layers. b-i) Shows the formation of a large hump, and b-ii) large hump defect evolution (Supplementary video 5). c-i) Shows the evolution of a small defect-induced hump and, c-ii) small hump defect evolution (Supplementary video 5). All scale bars are 200 μm.

created by the tidal-wave-like topology at the front of the melt pool. This wave travels to the back of the pool where undulations are observed due to the Rayleigh-Taylor (or Plateau-Rayleigh) instability [65], in addition to the lapping defect; note these undulation effects are amplified on subsequent build layers. The Rayleigh-Taylor instability describes an infinite column that is subjected to periodic instabilities (due to pressure differences) over a period of $2\pi R$ where R is the column radius [66]. The valley deepens as the laser beam remelts the material (at 144 ms), and then flattens as the laser beam continues to move away, because the liquid metal is being pushed towards the back of the melt pool *via* the Marangoni convection (184 ms). Fig 7cii shows the formation of spatter-induced humping, where a large spatter droplet is ejected and merged with the previously built track during scanning, causing small humps to form (Fig 7ci and ii).

3.6. Roughness analysis

Fig. 7a shows a decrease in the average R_a when the LED increases from 0.5 to 1 Jmm^{-1} (low range) due to two possible mechanisms: (i) when the melt pool size ratio (d/w) is large, this promotes Rayleigh-Taylor (or Plateau-Rayleigh) instability and balling formation (quantified later as shown by Fig. 8c). (2) Combined balling with a lack of fusion porosity and spatter (Fig. 6) generates a discontinuous track with a high side-skin roughness. [18,19,22] A minimum average R_a of 12 μm was achieved at an LED of ~1 Jmm^{-1}. As the LED continues to increase from 1 to 4 Jmm^{-1} (high range), severe metal vaporisation takes place, resulting in unstable keyhole-mode melting (quantified later as shown by Fig. 8c). Prior work hypothesised that for the mixing of hot and high-velocity vapour/argon (reaching up to 30 m/s) flowing above a fast-flowing melt pool (~ 4 m/s), the differences in flow velocities lead to the Kelvin-Helmholtz instability and hence hump formation [37], *i.e.* generating more ripple features at the track surface and increasing R_a of the track. The minimum R_a values calculated from the X-ray images are similar to those of the optical image at layer 10. The mean absolute percentage error (MAPE) between these two measurements is 0.04%: possibly owing to the filtering step during data processing.

Supplementary material related to this article can be found online at doi:10.1016/j.addma.2023.103809.

Parameters such as *P*, *v* and LED are shown to have an impact on the overall surface roughness of thin-wall build, though other parameters such as hatch distance have not been explored in this study. Several reports have observed that increasing hatch distance increases the overall roughness [3,67,68], which would affect the overall defect dynamics observed that are an onset of roughness, *i.e.*, lack of fusion and spatter (Section 3.3. - 3.4).

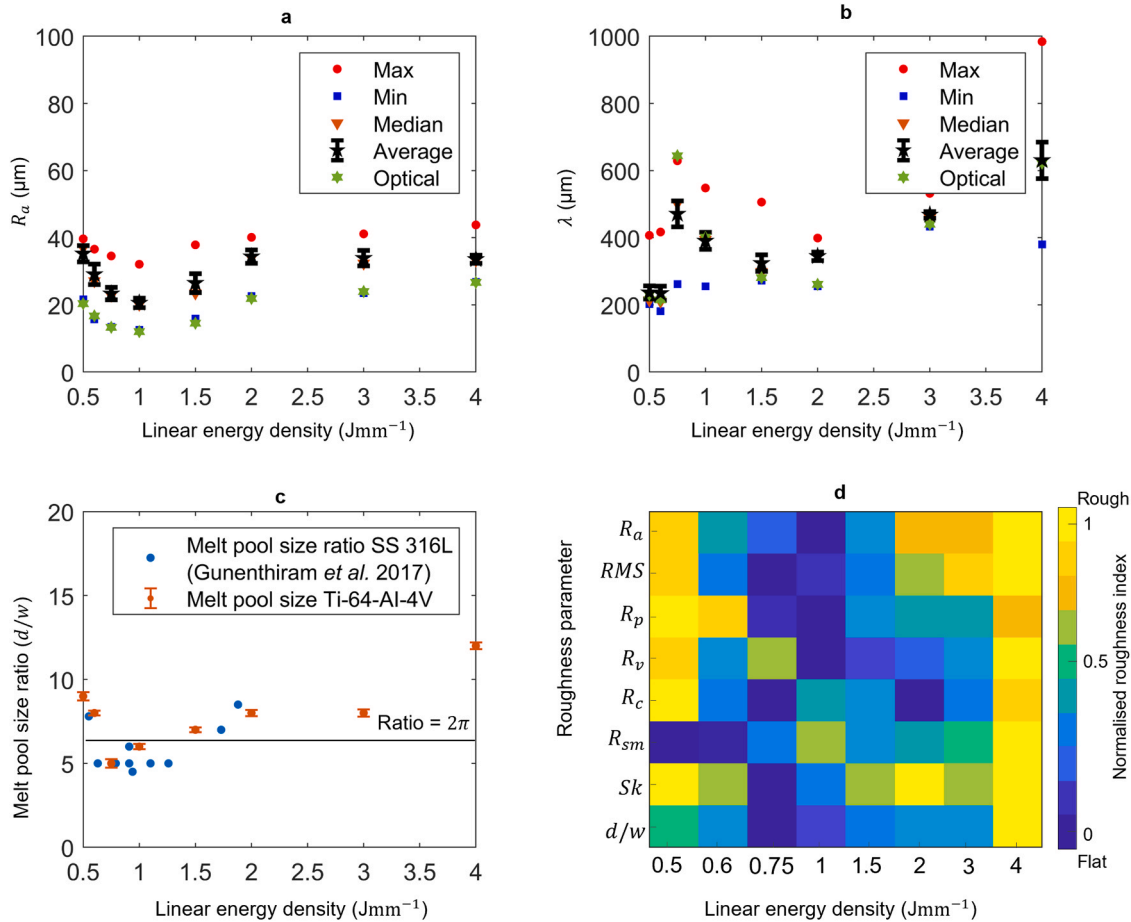Fig. 8b shows the λ increases in the low-range LED and decreases in

Fig. 8. Roughness quantification across different linear energy densities. a). Plot of the average arithmetical mean deviation (R_a) which includes maximum, minimum, median, and average values with error bars (standard error) from optical and X-ray images, see details in Supplementary Fig. 6a. b) A plot of the average waviness (λ) which includes maximum, minimum, median, average λ values with error bars (standard error) from optical and X-ray images, see details in Supplementary Fig. 6b. c). A scatter plot of the melt pool size ratio = depth (*d*) / width (*w*) versus the LED for (1) Ti-6Al-4V alloy and SS 316 L (after [66]). The black line divides the stable and unstable humping zone below and above the threshold, respectively. d). A normalised colourmap showing varying roughness parameters: average roughness (R_a); root mean square average (RMS); maximum profile peak height (R_p); maximum profile valley height (R_v); mean height (R_c); mean width (R_{sm}); skewness (Sk); and melt pool size ratio (d/w) for different LEDs. The values are normalised by maximum value of each row as shown in Supplementary Table 3 and Supplementary Table 4 ($X_{normalisation} = \frac{(X_i - X_{minimum})}{(X_{maximum} - X_{minimum})}$, where X_i: the actual value, $X_{minimum}$: minimum value on the row and $X_{maximum}$: maximum value in the row).

the high-range LED, an opposite trend to the R_a analysis; however, the highest λ is also achieved at an optimum LED of $\sim$1 Jmm^{-1}.

Fig. 8c compares two sets of results: (1) Ti-6Al-4V alloy (present study); and (2) stainless steel 316 L [66] under similar processing conditions. Ref [66] identified a threshold d/w ratio of 2π. Above the threshold, an unstable melt pool is formed with periodic humping, otherwise a stable melt pool is formed with a shallow amplitude and longer λ. Our results identify similar stable and unstable melt tracks, corroborating the results reported in ref [66].

Here, we propose a novel roughness selection matrix (Fig. 8d) to combine eight roughness parameters used in AM: (1) average roughness (R_a) [69]; (2) root mean square average (RMS) [70]; (3) maximum profile peak height (R_p) [26]; (4) maximum profile valley height (R_v) [71]; (5) mean height (R_c) [71]; (6) mean width (R_{sm}) [72]; (7) skewness (Sk) [71]; and (8) melt pool size ratio (d/w) ref. [66]. Each parameter has been normalised with a weighting between 0 and 1 representing low to high roughness (Supplementary Table 3 and Supplementary Table 4). The selected parameters represent roughness for a singular line as they are extracted from the *in situ* X-ray radiographs; however, the matrix presented has potential for additional singular valued aerial roughness measurements to be included. The R_a and λ have already been discussed extensively In Fig. 8a-b. RMS and R_a are both representations of surface roughness and the overall surface finish [73], and Fig. 8d shows the RMS follows a similar pattern to R_a (as demonstrated by Fig. 8a). There is a small difference in the RMS values in comparison to R_a , where RMS values are more sensitive to larger peaks/flaws within the surface and could be used as a comparison indicator to the R_a. The R_p and R_V values measure periodic undulation, and both values are used to calculate λ of the humps. The R_c and R_{sm} increase with LED indicating that λ increases and track height decreases, correlating to the finding in Fig. 8b and Fig. 2a. When the modulus of Sk is > 0, both peaks and valleys are prominent on the track surface, indicating a rough build surface. A higher Sk value means a lower number of asperities/peaks and valleys in the build, *i.e.,* a smoother build surface. A similar pattern arises for Sk and R_a, where LEDs of 0.75 and 1 Jmm^{-1} has the most symmetrical distribution of peaks and valleys, indicating low surface roughness. For each roughness parameter, we normalise all values using methods described in Supplementary Information (section G). The colour map denotes the average-built layer is flat as 1 and rough as 0. In the present study, the optimum printing parameter range to produce a flat surface is between LEDs of 0.75 and 1 Jmm^{-1}. Based on our findings, the end-users can tailor surface finish of a thin-wall build using the proposed roughness selection matrix as it considers both R_a and λ across the length scale of the LPBF process.

4. Conclusions

This study used *in situ* synchrotron X-ray imaging to investigate the evolution of the interlayer side-skin roughness and waviness and associated defect formation mechanisms during LPBF of TI-6Al-4V multilayer builds. The findings were supported by *ex situ* optical imaging and XCT results. A novel surface topology matrix was developed to describe surface features and defect formation mechanisms while effectively representing the overall geometrical build morphology and texture. The matrix can be used to find the desired surface finish and achieve better surface control under a layer-by-layer processing during LPBF. The following conclusions have been drawn:

1. Two key mechanisms were observed that affected the side-skin roughness and amplitude: (1) R_a decreased between an LED range of 0.5–1 Jmm^{-1}, due to a decreasing melt pool size ratio where the surface became smoother due to Plateau-Rayleigh and Kevin-Helmholtz instabilities and (2) R_a increased between a LED range of 1–4 Jmm^{-1} as metal vaporisation was more severe due to an

unstable keyhole melting mode. An optimal R_a of 12 μm was found to be at an LED of $\sim$1 Jmm^{-1}.

2. Using synchrotron X-ray imaging we observed the defect dynamics during LPBF and quantified their effects on each of the printed track quality. We found that defects that occur at: (1) LED range of 0.5–0.6 Jmm^{-1} include lack of fusion, spatter, balling and track interruption, which increase R_a; and (2) that regardless of the process parameter for LPBF printing, the single bi-directional multilayer printing lead to the formation of, lapping and humping defects, which also increasing R_a.

Author contribution

PDL, CLAL, MKT and AB conceived the research/project. CLAL and GS designed the experiments. All authors performed the beamtime, except MKT. AB performed data analysis and results in interpretation with the assistance of YH. AB, YH, CLAL, and PDL led the results interpretation and paper writing. GS performed powder size distribution analysis. SS performed μCT and AB analysed the results. AB, YH, GS performed surface roughness *ex situ* roughness results *via* Keyence.

CRediT authorship contribution statement

Alisha Bhatt: Conceptualisation, Methodology, Formal analysis, Investigation, Writing – original draft, Visualisation. **Yuze Huang:** Conceptualisation, Methodology, Investigation, Writing – review & editing. **Chu Lun Alex Leung:** Conceptualisation, Methodology, Investigation, Writing – review & editing, Funding acquisition. **Gowtham Soundarapandiyan:** Methodology, Investigation. **Sebastian Marussi:** Methodology, Investigation. **Saurabh Shah:** Methodology, Investigation. **Robert C. Atwood:** Resources, Supervision. **Michael E. Fitzpatrick:** Supervision, Conceptualisation, Resources, Writing – review & editing, Funding acquisition. **Manish K. Tiwari:** Supervision, Conceptualisation, Writing – review & editing, Funding acquisition. **Peter D. Lee:** Supervision, Conceptualisation, Investigation, Writing – review & editing, Funding acquisition.

Declaration of Competing Interest

The authors declare that they have no known competing financial interests or personal relationships that could have appeared to influence the work reported in this paper.

Data availability

Representative sample data is summarised in the figures (and supplementary data). Additional datasets generated and analysed during the study are available upon reasonable request through the corresponding authors due to the large size and volume of data acquired.

Acknowledgements

no competing financial interests.

Appendix A. Supporting information

Supplementary data associated with this article can be found in the online version at doi:10.1016/j.addma.2023.103809.

References

[1] M. Asherloo, Z. Wu, M. Heim, D. Nelson, M. Paliwal, A.D. Rollett, A. Mostafaei, Fatigue performance of laser powder bed fusion hydride-dehydride Ti-6Al-4V powder, Addit. Manuf. 59 (2022), 103117, https://doi.org/10.1016/j. addma.2022.103117.

[2] P.C. Collins, D.A. Brice, P. Samimi, I. Ghamarian, H.L. Fraser, Microstructural control of additively manufactured metallic materials, Annu. Rev. Mater. Res. 46 (2016) 63–91, https://doi.org/10.1146/annurev-matsci-070115-031816.

[3] C. Tang, K.Q. Le, C.H. Wong, Physics of humping formation in laser powder bed fusion, Int. J. Heat. Mass Transf. 149 (2020), https://doi.org/10.1016/j. ijheatmasstransfer.2019.119172.

[4] A. du Plessis, S. Beretta, Killer notches: the effect of as-built surface roughness on fatigue failure in AlSi10Mg produced by laser powder bed fusion, Addit. Manuf. 35 (2020), 101424, https://doi.org/10.1016/j.addma.2020.101424.

[5] W.J. Sames, F.A. List, S. Pannala, R.R. Dehoff, S.S. Babu, The metallurgy and processing science of metal additive manufacturing, Int. Mater. Rev. 61 (2016) 315–360, https://doi.org/10.1080/09506608.2015.1116649.

[6] B. Song, S. Dong, Q. Liu, H. Liao, C. Coddet, Vacuum heat treatment of iron parts produced by selective laser melting: microstructure, residual stress and tensile behavior, Mater. Des. 54 (2014) 727–733, https://doi.org/10.1016/j. matdes.2013.08.085.

[7] S. Leuders, M. Vollmer, F. Brenne, T. Tröster, T. Niendorf, Fatigue strength prediction for titanium alloy TiAl6V4 manufactured by selective laser melting, Metall. Mater. Trans. A Phys. Metall. Mater. Sci. 46 (2015) 3816–3823, https://doi. org/10.1007/s11661-015-2864-x.

[8] P. Edwards, M. Ramulu, Fatigue performance evaluation of selective laser melted Ti-6Al-4V, Mater. Sci. Eng. A 598 (2014) 327–337, https://doi.org/10.1016/j. msea.2014.01.041.

[9] S. Marimuthu, A. Triantaphyllou, M. Antar, D. Wimpenny, H. Morton, M. Beard, Laser polishing of selective laser melted components, Int. J. Mach. Tools Manuf. 95 (2015) 97–104, https://doi.org/10.1016/j.ijmachtools.2015.05.002.

[10] C. Ye, C. Zhang, J. Zhao, Y. Dong, Effects of post-processing on the surface finish, porosity, residual stresses, and fatigue performance of additive manufactured metals: a review, J. Mater. Eng. Perform. 30 (2021) 6407–6425, https://doi.org/ 10.1007/s11665-021-06021-7.

[11] K. Lietaert, A.A. Zadpoor, M. Sonnaert, J. Schrooten, L. Weber, A. Mortensen, J. Vleugels, Mechanical properties and cytocompatibility of dense and porous Zn produced by laser powder bed fusion for biodegradable implant applications, Acta Biomater. 110 (2020) 289–302, https://doi.org/10.1016/j.actbio.2020.04.006.

[12] M. Merola, S. Affatato, Materials for hip prostheses: a review of wear and loading considerations, Materials 12 (2019), https://doi.org/10.3390/ma12030495.

[13] H. Bhatt, T. Goswami, Implant wear mechanisms–basic approach, Biomed. Mater. 3 (2008) 42001, https://doi.org/10.1088/1748-6041/3/4/042001.

[14] O. Poncelet, M. Marteleur, C. van der Rest, O. Rigo, J. Adrien, S. Dancette, P. J. Jacques, A. Simar, Critical assessment of the impact of process parameters on vertical roughness and hardness of thin walls of AlSi10Mg processed by laser powder bed fusion, Addit. Manuf. 38 (2021), 101801, https://doi.org/10.1016/j. addma.2020.101801.

[15] X. Yan, C. Chang, D. Dong, S. Gao, W. Ma, M. Liu, H. Liao, S. Yin, Microstructure and mechanical properties of pure copper manufactured by selective laser melting, Mater. Sci. Eng. A 789 (2020), 139615, https://doi.org/10.1016/j. msea.2020.139615.

[16] J. Gockel, L. Sheridan, B. Koerper, B. Whip, The influence of additive manufacturing processing parameters on surface roughness and fatigue life, Int. J. Fatigue 124 (2019) 380–388, https://doi.org/10.1016/j.ijfatigue.2019.03.025.

[17] Z. Xiong, H. Li, H. Yang, Y. Yang, Y. Liu, L. Cui, X. Li, L. Masseling, L. Shen, S. Hao, Micro laser powder bed fusion of NiTi alloys with superior mechanical property and shape recovery function, Addit. Manuf. 57 (2022), 102960, https://doi.org/ 10.1016/j.addma.2022.102960.

[18] L. Cao, J. Li, J. Hu, H. Liu, Y. Wu, Q. Zhou, Optimization of surface roughness and dimensional accuracy in LPBF additive manufacturing Build platform, Opt. Laser Technol. 142 (2021), 107246, https://doi.org/10.1016/j.optlastec.2021.107246.

[19] L.N. Carter, V.M. Villapún, L. Grover, S.C. Cox, Exploring the duality of powder adhesion and underlying surface roughness in laser powder bed fusion processed Ti-6Al-4V, J. Manuf. Process 81 (2022) 14–26, https://doi.org/10.1016/j. jmapro.2022.06.057.

[20] Z.Y. Chua, I.H. Ahn, S.K. Moon, Process monitoring and inspection systems in metal additive manufacturing: status and applications, Int. J. Precis. Eng. Manuf. - Green. Technol. 4 (2017) 235–245, https://doi.org/10.1007/s40684-017-0029-7.

[21] P. Stief, J. Dantan, A. Etienne, A. Siadat, Study on improvement of surface roughness and induced residual stress for additively manufactured metal parts by abrasive flow machining, Fam., Procedia CIRP 71 (2018) 386–389, https://doi. org/10.1016/j.procir.2018.05.046.

[22] N. Gerdes, C. Hoff, J. Hermsdorf, S. Kaierle, L. Overmeyer, Hyperspectral imaging for prediction of surface roughness in laser powder bed fusion, Int. J. Adv. Manuf. Technol. 115 (2021) 1249–1258, https://doi.org/10.1007/s00170-021-07274-1.

[23] A. Townsend, N. Senin, L. Blunt, R.K. Leach, J.S. Taylor, Surface texture metrology for metal additive manufacturing: a review, Precis. Eng. 46 (2016) 34–47, https://doi.org/10.1016/j.precisioneng.2016.06.001.

[24] P. Ruano, L.L. Delgado, S. Picco, L. Villegas, F. Tonelli, M. Merlo, J. Rigau, D. Diaz, M. Masuelli, We are IntechOpen, the world ' s leading publisher of open access books built by scientists, for scientists TOP 1%, Intech (2016) 13, https://doi.org/ 10.5772/57353.

[25] J.C. Snyder, K.A. Thole, Understanding laser powder bed fusion surface roughness, in: J. Manuf. Sci. Eng. Trans, 142, ASME, 2020, https://doi.org/10.1115/ 1.4046504.

[26] M. Yonehara, C. Kato, T.T. Ikeshoji, K. Takeshita, H. Kyogoku, Correlation between surface texture and internal defects in laser powder-bed fusion additive manufacturing, Sci. Rep. 11 (2021) 1–10, https://doi.org/10.1038/s41598-021-02240-z.

[27] C.A. Brown, Roughness, Handb. Lubr. Tribol. Vol. II Theory Des. Second Ed. 123 (2012) 3-1-3–13. https://doi.org/10.1201/b12265.

[28] H. Zhongxiang, Z. Lei, T. Jiaxu, M. Xuehong, S. Xiaojun, Evaluation of three-dimensional surface roughness parameters based on digital image processing, Int. J. Adv. Manuf. Technol. 40 (2009) 342–348, https://doi.org/10.1007/s00170-007-1357-5.

[29] L. Caprio, A.G. Demir, B. Previtali, Observing molten pool surface oscillations during keyhole processing in laser powder bed fusion as a novel method to estimate the penetration depth, Addit. Manuf. 36 (2020), 101470, https://doi.org/10.1016/ j.addma.2020.101470.

[30] L. Sinclair, C.L.A. Leung, S. Marussi, S.J. Clark, Y. Chen, M.P. Olbinado, A. Rack, J. Gardy, G.J. Baxter, P.D. Lee, In situ radiographic and ex situ tomographic analysis of pore interactions during multilayer builds in laser powder bed fusion, Addit. Manuf. 36 (2020), 101512, https://doi.org/10.1016/j.addma.2020.101512.

[31] T. Liu, C.S. Lough, H. Sehhat, Y.M. Ren, P.D. Christofides, E.C. Kinzel, M.C. Leu, In-situ infrared thermographic inspection for local powder layer thickness measurement in laser powder bed fusion, Addit. Manuf. 55 (2022), 102873, https://doi.org/10.1016/j.addma.2022.102873.

[32] Z. Snow, L. Scime, A. Ziabari, B. Fisher, V. Paquit, Observation of spatter-induced stochastic lack-of-fusion in laser powder bed fusion using in situ process monitoring, Addit. Manuf. 61 (2023), 103298, https://doi.org/10.1016/j. addma.2022.103298.

[33] M. Drakopoulos, Engineering science at the I12 beamline at diamond light source, Synchrotron Radiat. N. 30 (2017) 41–47, https://doi.org/10.1080/ 08940886.2017.1316131.

[34] C.L.A. Leung, S. Marussi, M. Towrie, R.C. Atwood, P.J. Withers, P.D. Lee, The effect of powder oxidation on defect formation in laser additive manufacturing, Acta Mater. 166 (2019) 294–305, https://doi.org/10.1016/j.actamat.2018.12.027.

[35] Y. Chen, S.J. Clark, C.L.A. Leung, L. Sinclair, S. Marussi, M.P. Olbinado, E. Boller, A. Rack, I. Todd, P.D. Lee, In-situ synchrotron imaging of keyhole mode multi-layer laser powder bed fusion additive manufacturing, Appl. Mater. Today 20 (2020), 100650, https://doi.org/10.1016/j.apmt.2020.100650.

[36] J. Lawrence, A.A. Peligrad, E. Zhou, L. Li, D. Morton, Prediction of melt depth in selected architectural materials during high-power diode laser treatment, Opt. Lasers Eng. 35 (2001) 51–62, https://doi.org/10.1016/S0143-8166(00)00099-3.

[37] C.L.A. Leung, D. Luczyniec, E. Guo, S. Marussi, R.C. Atwood, M. Meisnar, B. Saunders, P.D. Lee, Quantification of interdependent dynamics during laser additive manufacturing using x-ray imaging informed multi-physics and multiphase simulation, Adv. Sci. 9 (2022) 1–15, https://doi.org/10.1002/ advs.202203546.

[38] L. Sinclair, C.L.A. Leung, S. Marussi, S.J. Clark, Y. Chen, M.P. Olbinado, A. Rack, J. Gardy, G.J. Baxter, P.D. Lee, In situ radiographic and ex situ tomographic analysis of pore interactions during multilayer builds in laser powder bed fusion, Addit. Manuf. 36 (2020), 101512, https://doi.org/10.1016/j.addma.2020.101512.

[39] C.L.A. Leung, S. Marussi, R.C. Atwood, M. Towrie, P.J. Withers, P.D. Lee, In situ X-ray imaging of defect and molten pool dynamics in laser additive manufacturing, Nat. Commun. 9 (2018) 1–9, https://doi.org/10.1038/s41467-018-03734-7.

[40] Y. Huang, T.G. Fleming, S.J. Clark, S. Marussi, K. Fezzaa, J. Thiyagalingam, C. A. Leung, P.D. Lee, Keyhole fluctuation and pore formation mechanisms during laser powder bed fusion additive manufacturing, Nat. Commun. 13 (2022) 1–11, https://doi.org/10.1038/s41467-022-28694-x.

[41] I. Yadroitsev, A. Gusarov, I. Yadroitsava, I. Smurov, Single track formation in selective laser melting of metal powders, J. Mater. Process. Technol. 210 (2010) 1624–1631, https://doi.org/10.1016/j.jmatprotec.2010.05.010.

[42] C.A. Schneider, W.S. Rasband, K.W. Eliceiri, NIH image to imageJ: 25 years of image analysis, Nat. Methods 9 (2012) 671–675, https://doi.org/10.1038/ nmeth.2089.

[43] J.D. Hunter, a 2D G, Comput. Sci. Eng. 9 (2007) 90–95.

[44] G. Van Rossum, F.L. Drake Jr, The python language reference: expressions, Python Ref. Man. (2009) id12. ⟨https://docs.python.org/3/reference/%0Ahttps://docs. python.org/3/reference/expressions.html#⟩.

[45] O.A. Yakimenko, Symbolic Math Toolbox, Eng. Comput. Model. MATLAB®/ Simulink®. (2011) 285–336. https://doi.org/10.2514/5.9781600867828.0285. 0336.

[46] J.A. Seibert, J.M. Boone, K.K. Lindfors, Flat-field correction technique for digital detectors, Med. Imaging 1998 Phys, Med. Imaging 3336 (1998) 348, https://doi. org/10.1117/12.317034.

[47] A.L.C. Kwan, J.A. Seibert, J.M. Boone, An improved method for flat-field correction of flat panel x-ray detector, Med. Phys. 33 (2006) 391–393, https://doi.org/10.1118/1.2163388.

[48] T. Ehret, P. Arias, Implementation of VBM3D and some variants, Image Process. Line 11 (2021) 374–395, https://doi.org/10.5201/ipol.2021.340.

[49] D. Liu, J. Yu, Otsu method and K-means, Proc. - 2009 9th Int. Conf. Hybrid. Intell. Syst. HIS 2009 1 (2009) 344–349, https://doi.org/10.1109/HIS.2009.74.

[50] E.A. Sobie, An introduction to MATLAB, Sci. Signal 4 (2011) tr7, https://doi.org/10.1126/scisignal.2001984.

[51] D. Janecki, Gaussian filters with profile extrapolation, Precis. Eng. 35 (2011) 602–606, https://doi.org/10.1016/j.precisioneng.2011.04.003.

[52] Y.B. Yuan, T.V. Vorburger, J.F. Song, T.B. Renegar, A simplified realization for the Gaussian filter in surface metrology, Int. Colloq Surf., Chemnitz (2000), 133–133, ⟨https://www.nist.gov/sites/default/files/documents/calibrations/10-srfce.pdf⟩.

[53] Gaussian Regression Filters, Comput. Surf. Roundness Metrol., in: Comput. Surf. Roundness Metrol., Springer London, London, 2009, pp. 67–76, https://doi.org/10.1007/978-1-84800-297-5_9.

[54] J. Raja, B. Muralikrishnan, S. Fu, Recent advances in separation of roughness, waviness and form, Precis. Eng. 26 (2002) 222–235, https://doi.org/10.1016/S0141-6359(02)00103-4.

[55] B. Whip, L. Sheridan, J. Gockel, The effect of primary processing parameters on surface roughness in laser powder bed additive manufacturing, Int. J. Adv. Manuf. Technol. 103 (2019) 4411–4422, https://doi.org/10.1007/s00170-019-03716-z.

[56] W. Yuan, H. Chen, T. Cheng, Q. Wei, Effects of laser scanning speeds on different states of the molten pool during selective laser melting: simulation and experiment, Mater. Des. 189 (2020), 108542, https://doi.org/10.1016/j.matdes.2020.108542.

[57] P. Tang, S. Wang, H. Duan, M. Long, Y. Li, S. Fan, D. Chen, The formation of humps and ripples during selective laser melting of 316l stainless steel, Jom 72 (2020) 1128–1137, https://doi.org/10.1007/s11837-019-03987-7.

[58] Z. Wang, K. Walayat, M. Liu, Ripple formation and whole-process modelling of selective laser melting BIC-ESAT & state key laboratory for turbulence and complex systems, college of engineering, BIC-ESAT & state key laboratory for turbulence and complex systems, Coll. Eng. (2018) 118–121.

[59] M. Seiler, A. Patschger, J. Bliedtner, Investigations of welding instabilities and weld seam formation during laser microwelding of ultrathin metal sheets, J. Laser Appl. 28 (2016), 022417, https://doi.org/10.2351/1.4944446.

[60] W. Ameen, A. Al-Ahmari, M.K. Mohammed, Self-supporting overhang structures produced by additive manufacturing through electron beam melting, Int. J. Adv. Manuf. Technol. 104 (2019) 2215–2232, https://doi.org/10.1007/s00170-019-04007-3.

[61] C.L.A. Leung, R. Tosi, E. Muzangaza, S. Nonni, P.J. Withers, P.D. Lee, Effect of preheating on the thermal, microstructural and mechanical properties of selective electron beam melted Ti-6Al-4V components, Mater. Des. 174 (2019), 107792, https://doi.org/10.1016/j.matdes.2019.107792.

[62] S. Ly, A.M. Rubenchik, S.A. Khairallah, G. Guss, J. Manyalibo, Metal vapor micro-jet controls material redistribution in laser powder bed fusion additive manufacturing, (2017) 1–12. https://doi.org/10.1038/s41598-017-04237-z.

[63] A.A. Martin, N.P. Calta, S.A. Khairallah, J. Wang, P.J. Depond, A.Y. Fong, V. Thampy, G.M. Guss, A.M. Kiss, K.H. Stone, C.J. Tassone, J. Nelson Weker, M. F. Toney, T. van Buuren, M.J. Matthews, Dynamics of pore formation during laser powder bed fusion additive manufacturing, Nat. Commun. 10 (2019) 1–10, https://doi.org/10.1038/s41467-019-10009-2.

[64] S. Patel, A. Rogalsky, M. Vlasea, Towards understanding side-skin surface characteristics in laser powder bed fusion, J. Mater. Res 35 (2020) 2055–2064, https://doi.org/10.1557/jmr.2020.125.

[65] N. Ivanova, V. Gugleva, M. Dobreva, I. Pehlivanov, S. Stefanov, V. Andonova, We are IntechOpen, the world ' s leading publisher of Open Access books Built by scientists, for scientists TOP 1%, Intech. i (2016) 13.

[66] V. Gunenthiram, P. Peyre, M. Schneider, M. Dal, V. Gunenthiram, P. Peyre, M. Schneider, M. Dal, F. Coste, Analysis of laser – melt pool – powder bed interaction during the selective laser melting of a stainless steel To cite this version: HAL Id: hal-01664637, (2017).

[67] Z. Dong, Y. Liu, W. Wen, J. Ge, J. Liang, Effect of hatch spacing on melt pool and as-built quality during selective laser melting of stainless steel: modeling and experimental approaches, Materials 12 (2018), https://doi.org/10.3390/ma12010050.

[68] A.M. Vilardell, I. Yadroitsev, I. Yadroitsava, M. Albu, N. Takata, M. Kobashi, P. Krakhmalev, D. Kouprianoff, G. Kothleitner, A. du Plessis, Manufacturing and characterization of in-situ alloyed Ti6Al4V(ELI)-3 at% Cu by laser powder bed fusion, Addit. Manuf. 36 (2020), https://doi.org/10.1016/j.addma.2020.101436.

[69] T.R. Thomas, Characterization of surface roughness, Precis. Eng. 3 (1981) 97–104, https://doi.org/10.1016/0141-6359(81)90043-X.

[70] M. Sedlaček, P. Gregorčič, B. Podgornik, Use of the roughness parameters ssk and sku to control friction—a method for designing surface texturing, Tribol. Trans. 60 (2017) 260–266, https://doi.org/10.1080/10402004.2016.1159358.

[71] J. Józwik, D. Ostrowski, R. Milczarczyk, G.M. Krolczyk, Analysis of relation between the 3D printer laser beam power and the surface morphology properties in Ti-6Al-4V titanium alloy parts, J. Braz. Soc. Mech. Sci. Eng. 40 (2018), https://doi.org/10.1007/s40430-018-1144-2.

[72] J.C. Fox, S.P. Moylan, B.M. Lane, Effect of process parameters on the surface roughness of overhanging structures in laser powder bed fusion additive manufacturing, Procedia CIRP 45 (2016) 131–134, https://doi.org/10.1016/j.procir.2016.02.347.

[73] C.J.Luis Pérez, Analysis of the surface roughness and dimensional accuracy capability of fused deposition modelling processes, Int. J. Prod. Res. 40 (2002) 2865–2881, https://doi.org/10.1080/00207540210146099.